The Astrophysical Journal Supplement Series, 275:29 (12pp), 2024 December https://doi.org/10.3847/1538-4365/ad8b40

An Upgraded Line List for Radiative Transitions between the $B\,^2\Sigma^+$, $A\,^2\Pi$, and $X\,^2\Sigma^+$ States of the CN Radical

S. V. Kozlov[1], V. A. Terashkevich[1], E. A. Pazyuk[1], A. V. Stolyarov[1], S. N. Yurchenko[2], and J. Tennyson[2]
[1] Department of Chemistry, Lomonosov Moscow State University, 119991, Moscow, Leninskie gory 1/3, Russia; avstol@phys.chem.msu.ru
[2] Department of Physics and Astronomy, University College London, Gower St., London WC1E 6BT, UK; s.yurchenko@ucl.ac.uk
Received 2024 July 29; revised 2024 October 5; accepted 2024 October 13; published 2024 November 19

Abstract

The global mass-invariant coupled-channel deperturbation model of the $B\,^2\Sigma^+$, $A\,^2\Pi$, and $X\,^2\Sigma^+$ states of the CN radical, which reproduces the overall rovibronic term values of mutually perturbed levels with almost spectroscopic accuracy, has been utilized to produce complete line lists of radiative transitions between the $X\,^2\Sigma^+$, $B\,^2\Sigma^+$, and $A\,^2\Pi_{1/2;3/2}$ states of CN isotopologues. The Einstein A emission coefficients generated for the $A-X$, $B-X$, and $B-A$ transitions provide both lifetimes of the excited states as well as the $B\rightarrow A/X$ branching ratios. The *ab initio* permanent and transition dipole moments required are revisited within the framework of the multireference configuration interaction and of the averaged coupled-pair functional methods. An upgraded line list is provided in ExoMol format and employed to simulate intensity distribution into the high-temperature air plasma $B\rightarrow X$ and $A\rightarrow X$ spectra as well as in the rotational resolved $B\rightarrow X/A$ emission bands undergoing strong local $B\sim A\sim X$ perturbations. A comparison with laboratory and astronomical spectra shows that the present line list significantly improves the treatment of both locally perturbed and highly excited rotational levels of the $B\sim A\sim X$ complex.

Unified Astronomy Thesaurus concepts: Molecular data (2259); Molecular spectroscopic constants (2260); Molecular spectroscopy (2095); Exoplanet atmospheres (487); Stellar atmospheric opacity (1585)

Materials only available in the online version of record: tar.gz file

1. Introduction

The diatomic CN radical is formed in a variety of high-temperature aeronomic, cosmic, and laboratory environments containing of carbon and nitrogen atoms. Optical transitions between the lowest three doublet states of the CN radical, $B\,^2\Sigma^+-X\,^2\Sigma^+$ (violet system), $A\,^2\Pi-X\,^2\Sigma^+$ (red system), and $B\,^2\Sigma^+-A\,^2\Pi$ (LeBlanc system), are observed in many cosmic objects, such as interstellar clouds (A. McKellar 1940; S. R. Federman et al. 1984), comets (N. Hänni et al. 2020; N. Fray et al. 2005), as well as carbon stars (G. R. Wiedemann et al. 1991) and potentially in the atmospheres of exoplanets. Observation of astrophysical CN spectra are important for monitoring star formation processes (R. Riffel et al. 2007) and for an alternative determination of the cosmic microwave background radiation temperature $T_{\rm CMBR}$ by means of relative intensity measurements of several low-lying lines in the $X\rightarrow B$ (0,0) absorption band (K. C. Roth et al. 1993; K. Słyk et al. 2008; A. M. Ritchey et al. 2011; S. Leach 2012; S. Harrison et al. 2013).

CN molecules often arise as a result of convective thermal ablation of spacecraft in hypersonic air flows during their entry into planetary atmospheres such as those of Earth and Titan (S. Löhle et al. 2011) and certain ground-based hypersonic tests based on strong shock-wave facilities (D. Bose et al. 2006). CN radicals can be formed in air using laser-induced breakdown spectroscopy (LIBS; S. J. Mousavi et al. 2016) and flash photolysis (R. Engleman 1974) of carbon-containing organic and inorganic samples. The presence of the CN radical in the resulting plasma expands its high-temperature diagnostic possibilities up to $T=10{,}000$ K, assuming local thermodynamic equilibrium (LTE), or distinguishing nonequilibrium rotational and vibrational populations of the excited levels observed in the $B\rightarrow X$ and $A\rightarrow X$ rovibronic emission transitions (C. G. Parigger et al. 2015).

Developing nonequilibrium temperature and speciation optical diagnostics of cold gas-phase and plasma environments unambiguously require high-fidelity spectroscopic line lists such as those provided by the HITRAN (I. E. Gordon et al. 2022), ExoMol (J. Tennyson et al. 2020), and LIFBASE[3] electronic databases. These databases provide rovibronic transition wavenumbers, ν_{ij}, accompanied by the corresponding Einstein coefficients, A_{ij}, and radiative lifetimes, τ_i, for the isolated molecules of interest which are valid for a wide range of internal excitations. In particular, the Molecular Line Lists, Intensities and Spectra (MoLLIST) database (P. F. Bernath 2020) provides spectral information of the CN radical calculated (J. S. A. Brooke et al. 2014; C. Sneden et al. 2014) using Western's PGOPHER program (C. M. Western 2017) for the rovibronic $B-X$ ($\upsilon_B\in[0,\ 22]$, $\upsilon_X\in[0,\ 15]$), and $A-X$ ($\upsilon_A\in[0,\ 22]$, $\upsilon_X\in[0,\ 15]$) transitions as well as for rovibrational transitions limited by ground X-state vibrational $\upsilon_X\in[0,\ 15]$ levels. The MoLLIST model provides highly accurate transition wavenumbers for the most abundant $^{12}C^{14}N$ and minor $^{13}C^{14}N$ and $^{12}C^{15}N$ isotopologues. However, the effective Hamiltonian approach (J. M. Brown et al. 1979) implemented in PGOPHER does not extrapolate reliably and cannot generate accurate line lists far outside the limits of the domain probed experimentally.

Nowadays, the most reliable diatomic line strengths are determined by means of high-level *ab initio* calculated permanent (PDM) and transition (TDM) dipole moments combined with the corresponding semiempirical rovibrational wave functions generated using the adiabatic and/or non-adiabatic approximation. During the past decades the required *ab initio* PDM functions for the $X\,^2\Sigma^+$, $A\,^2\Pi$, and $B\,^2\Sigma^+$ states

[3] https://www.sri.com/engage/products-solutions/lifbase

of CN and relevant spin-allowed $B-A$, $B-X$, and $A-X$ TDM functions have been recalculated many times by means of the robust quantum-chemistry methods (H. Lavendy et al. 1984; C. W. J. Bauschlicher et al. 1988; P. J. Knowles et al. 1988; S. R. Langhoff & C. W. J. Bauschlicher 1989; H. J. Kulik et al. 2009; J. S. A. Brooke et al. 2014; Y. Yin et al. 2018; L. Liu & X. Cheng 2022). However, these TDM have proved to be not completely reliable since some calculated radiative properties of the states treated systematically diverge from their experimental measurements (R. Thomson & F. W. Dalby 1968; P. F. Bernath 2020).

Recently, a comprehensive TriHybrid (experimental–perturbative–variational) spectroscopic model was developed by A.-M. Syme & L. K. McKemmish (2021) for the $B\sim A\sim X$ complex of CN and used to compile a comprehensive line list that includes energy levels obtained by the processing of experimental wavenumbers using the measured active vibration rotation energy levels (MARVEL) procedure (A.-M. Syme & L. K. McKemmish 2020), within the framework of a conventional effective Hamiltonian approach method as well as due to the rigorous coupled-channel (CC) deperturbation analysis realized with help of the DUO variational nuclear motion program (S. N. Yurchenko et al. 2016). The TriHybrid line list created in the ExoMol format is recommended for simulating the optical spectra of the CN radical in a wide range of environmental conditions. However, the CC deperturbation model developed by A.-M. Syme & L. K. McKemmish (2021) was not able to accurately reproduce the experimental term values of both regular and local perturbed levels of the molecule with spectroscopic accuracy, particularly for highly excited rotational levels. Thus, the radiative parameters of the TriHybrid line list are probably not accurate enough, particularly for use in hot environments where high-lying rotational states are important. Thus, for example, application of TriHybrid for modeling the high-temperature LIBS emission spectrum of the violet $B-X(\upsilon_B,\upsilon_X)$ system (the diagonal $\upsilon_B=\upsilon_X$ sequence) reveals a clear discrepancy in the spectral region of the (2, 2), (3, 3), and (4, 4) band heads (C. G. Parigger 2023).

In the present work (PW), the global mass-invariant CC deperturbation model (V. A. Terashkevich et al. 2021, 2022), which reproduces the overall rovibronic term values of mutually perturbed levels of the $B\,^2\Sigma^+$, $A\,^2\Pi$, and $X\,^2\Sigma^+$ states of the CN radical with almost spectroscopic accuracy, has been utilized to computed line lists for three isotopologues of CN, $^{12}C^{14}N$, $^{13}C^{14}N$, and $^{12}C^{15}N$, covering radiative transitions between the $X\,^2\Sigma^+$, $B\,^2\Sigma^+$, and $A\,^2\Pi_{1/2;3/2}$ electronic states. The line lists contain accurate rovibronic transition wavenumbers and Einstein A coefficients for the $A-X$, $B-X$, and $B-A$ bands, as well as radiative lifetimes and the $B\rightarrow A/X$ branching ratios. The *ab initio* PDM and TDM curves required were revisited within the framework of the multireference configuration interaction (MR-CISD) and of the averaged coupled-pair functional (MR-ACPF) methods exploiting the all-electron *d-aug-cc*-pV5Z and *aug-cc*-pCV(5, 6)Z basis sets. The line lists, which we call KTPSYT, are presented in the ExoMol format; they are employed to simulate emission spectra of of the laser-induced air plasma in the $B\rightarrow X$ and $A\rightarrow X$ bands, non-LTE spectra of $A-X$, spectra of the $B\rightarrow X/A$ system undergoing strong local $B\sim A\sim X$ perturbations, as well as observed stellar spectra.

2. The Computational Pathway

2.1. Eigenvalues and Eigenfunctions

Nonadiabatic rovibronic term values (eigenvalues) $E_i^{\rm CC}$ and the relevant four-component vibrational wave functions (eigenfunctions) $\mathbf{\Phi}_i^{\rm CC}\equiv||\phi_i^B,\,\phi_i^{A_{1/2}},\,\phi_i^{A_{3/2}},\,\phi_i^X||$ corresponding to e/f parity bound levels of the mutually perturbed $X\,^2\Sigma^+$, $A\,^2\Pi_{1/2}$, $A\,^2\Pi_{3/2}$, and $B\,^2\Sigma^+$ states of the CN radical were obtained by solving 4×4 coupled-channel (CC) equations (S. N. Yurchenko et al. 2016; V. A. Terashkevich et al. 2022):

$$\left(-\boldsymbol{I}\frac{\hbar^2d^2}{2\mu dR^2}+\boldsymbol{V}^{e/f}(R;\,\mu,\,J)-\boldsymbol{I}E_i^{\rm CC}\right)\mathbf{\Phi}_i^{\rm CC}(R)=0$$
$$\mathbf{\Phi}_i^{\rm CC}(0)=\mathbf{\Phi}_i^{\rm CC}(+\infty)=0 \qquad (1)$$

with the normalization condition:

$$\sum_{k=1}^{4}P_i^k=1;\quad P_i^k=\langle\phi_i^k|\phi_i^k\rangle_R;$$
$$i,\,k\in[B\,^2\Sigma^+,\,A\,^2\Pi_{1/2},\,A\,^2\Pi_{3/2},\,X\,^2\Sigma^+]. \qquad (2)$$

Hereafter, P_i^k is the fractional population of the ith level of the $B\sim A\sim X$ complex with the particular (fixed) $J(N)$ value, $\boldsymbol{I}$ is the identity matrix, and μ is the reduced molecular mass. J $(=N\pm1/2)$ is the angular momentum quantum number, which is considered to be good as the hyperfine structure of the molecule is completely neglected in the present study.

The $\boldsymbol{V}^{e/f}(R;\mu,\,J)$ term in the CC Equation (1) is the symmetric 4×4 matrix of potential energy being an explicit parametric function of μ and J. Comprehensive information about diagonal and off-diagonal matrix elements of the $\boldsymbol{V}$-matrix is given by V. A. Terashkevich et al. (2022), where three mass-invariant sets of the deperturbed structure parameters as functions of internuclear distance R (including potential energy curves, spin–orbit and electron-rotational coupling matrix elements, and the Λ-doubling p, q (in the $A^2\Pi$ state) and spin-rotational γ parameters (in both $B^2\Sigma^+$ and $X^2\Sigma^+$ states) were determined.

We note that electronic and vibrational assignment of the mutually perturbed rovibronic levels belonging to the $B\sim A\sim X$ complex is often ambiguous since numerous nonadiabatic interactions mix electronic states and break down the *oscillation* theorem conditions (V. I. Pupyshev et al. 2010). Here assignments were made approximately based on the P_i^k values of fractional population as follows. For each fixed J and parity set, the calculated rovibronic term values of the nonadiabatic levels were part assigned to X, $A_{1/2}$, $A_{3/2}$, and B states according to the largest P_i^k. Then, the resulting subsets were reordered to give increasing term values and the vibrational quantum numbers renumerated starting from the lowest vibrational energy term with $\upsilon_i=0$ until maximal energy assuming the *oscillation* theorem still works correctly.

2.2. Transition Matrix Elements and Einstein A Coefficients

The Einstein $A_{i\rightarrow j}$ coefficients of spontaneous emission (in s^{-1}) from the upper i to lower j level of the $B\sim A\sim X$ complex of CN were calculated (J. S. A. Brooke et al. 2014) as

$$A_{i\rightarrow j}=3.13618932\times10^{-7}\nu_{ij}^3\left(\sum_{k=1}^{4}\sum_{l=1}^{4}M_{ij}^{kl}\right)^2, \qquad (3)$$

where the summation is performed over all fraction components of the upper and lower nonadiabatic states. Hereafter, $\nu_{ij} = E_i^{CC} - E_j^{CC}$ is the $i \rightarrow j$ transition wavenumber (in cm^{-1}),

$$M_{ij}^{kl} = W_{ij}^{kl} \langle \phi_i^k | d^{kl} | \phi_j^l \rangle_R \quad (4)$$

is the rovibronic transition matrix elements (in debye), $d^{kl}(R)$ is the permanent (if $k = l$) or transition ($k \neq l$) dipole moment functions (in debye), and W_{ij}^{kl} are the dimensionless rotational factors defined by the Wigner 3j symbols (see Equation (18) of J. K. G. Watson 2008):

$$W_{ij}^{kl} = \frac{1 + s(-1)^{J_i - J_j + 1}}{2} \sqrt{2J_j + 1} \begin{pmatrix} J_i & 1 & J_j \\ -\Omega_k & \Delta\Lambda & \Omega_l \end{pmatrix}, \quad (5)$$

where $\Delta\Lambda = \Lambda_k - \Lambda_l = \Omega_k - \Omega_l$. The parameter $s = 1$ for the $e \leftrightarrow e$ and $f \leftrightarrow f$ transitions and $s = -1$ for the $e \leftrightarrow f$ transitions. Thus, in accordance with the strong selection rules defined by Equation (5), one has 6, 12, and 24 rotational branches for $\Sigma^+ \leftrightarrow \Sigma^+$, $\Sigma^+ \leftrightarrow \Pi$, and $\Pi \leftrightarrow \Pi$ transitions, respectively.

2.3. Permanent and Transition Dipole Moments

The required permanent dipole moments $d^{kk}(R)$ of the isolated X, A, and B states and spin-allowed $A - X$, $B - X$, and $B - A$ transition dipole moments $d^{kl}(R)$ were *ab initio* evaluated in the range of internuclear distances $R \in [0.7, 4.0]$ Å on a uniform grid of 0.05 Å.

The present electronic structure calculation was performed for the following reasons. First, to ensure self-consistent relative signs for the TDM curves with the corresponding ones of the nonadiabatic (spin–orbit and L-uncoupling) matrix elements (A. T. Patrascu et al. 2014; V. A. Terashkevich et al. 2021) used for the global deperturbation treatment of the $B \sim A \sim X$ complex. Second, to monitor convergence of the resulting *ab initio* functions with respect to the atomic basis set expansion and treatment of electron correlation.

The active space consisted of $4a_1$, $2b_1$, and $2b_2$ molecular orbitals (MOs) corresponding to the C_{2v} symmetry point group; the two lowest a_1 closed-shell orbitals were doubly occupied in all reference configurations and no orbitals were frozen. The original self-consistent field MOs were optimized using a state-averaged complete active space self-consistent field procedure and then used for the internally contracted multireference configuration interaction (*ic*-MR-CISD) calculations based on the all-electron *d-aug-cc*-pV5Z basis set for both carbon and nitrogen atoms. Both PDM and TDM functions were computed from the *ic*-MR-CISD wave functions in the length representation.

An alternative calculation was additionally performed for the lowest $X\,^2\Sigma^+$ and $A\,^2\Pi$ states within the framework of the MR-ACPF method exploiting the *aug-cc*-pCV($n = 5, 6$)Z basis sets. All electronic structure calculations were conducted using the MOLPRO quantum-chemistry package[4] (H.-J. Werner et al. 2012).

2.4. Oscillator Strengths, Branching Ratios, and Radiative Lifetimes

The computed Einstein A coefficients were used to calculate the dimensionless oscillator strengths, f_{ij}, and branching ratios, R_{ijk}, of rovibronic $i - j$ and $i - k$ transitions

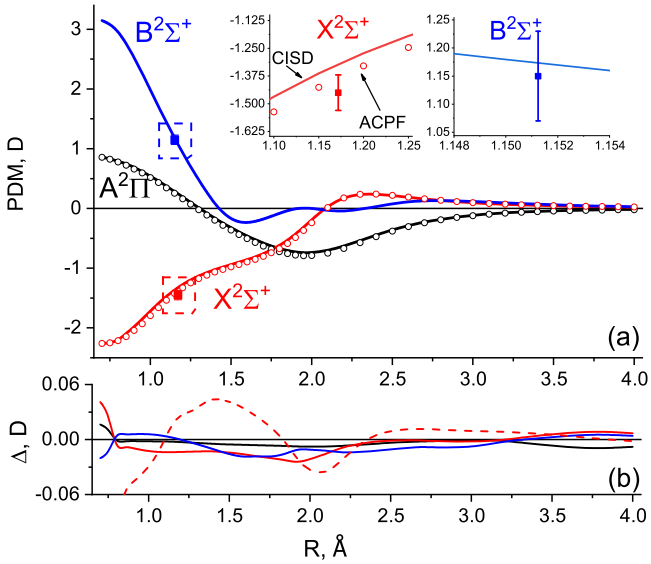

Figure 1. (a) *Ab initio* permanent dipole moment curves (in debye) obtained within the framework of *ic*-MR-CISD/d-aug-cc-pV5Z (solid lines) and MR-ACPF/aug-cc-pCV5Z (open circles) calculations for the $X\,^2\Sigma^+$, $A\,^2\Pi$, and $B\,^2\Sigma^+$ states of CN. The insets represent the zoomed PDM functions of the $X\,^2\Sigma^+$ and $B\,^2\Sigma^+$ states located near their equilibrium distances, along with their experimental counterparts (R. Thomson & F. W. Dalby 1968). (b) The difference between the present *ic*-MR-CISD/d-aug-cc-pV5Z and previous *ab initio* PDM functions: dashed (J. S. A. Brooke et al. 2014) and solid (A. -M. Syme & L. K. McKemmish 2021) lines, respectively.

(J. S. A. Brooke et al. 2014):

$$f_{ij} = 1.49919368 \frac{2J_i + 1}{2J_j + 1} \frac{A_{ij}}{\nu_{ij}^2} \quad (6)$$

$$R_{ijk} = \frac{A_{ij}}{A_{ik}} \quad (7)$$

as well as radiative lifetimes τ_i (in seconds) of the upper ith levels:

$$\frac{1}{\tau_i} = \sum_j A_{ij}, \quad (8)$$

where the summation is performed over all lower-lying rovibronic j-levels satisfying the energy condition $E_i^{CC} > E_j^{CC}$. The i, j, and k indexes above mean the $X\,^2\Sigma^+$, $B\,^2\Sigma^+$, $A\,^2\Pi_{1/2}$, and $A\,^2\Pi_{3/2}$ electronic states as well as e/f symmetry, rotational $J(N)$, and vibrational υ quantum numbers of the rovibronic levels involved.

3. Results and Discussion

3.1. Ab Initio PDM and TDM Functions

The resulting PDM functions obtained for the $X\,^2\Sigma^+$, $A\,^2\Pi$, and $B\,^2\Sigma^+$ states within the framework of the *ic*-MR-CISD and MR-ACPF methods are shown on Figure 1(a). The two *ab initio* methods demonstrated very good agreement with each other for the ground $X\,^2\Sigma^+$ and first excited $A\,^2\Pi$ states, for which the MR-ACPF procedure was well converged. For instance, the difference between the MR-CISD and MR-ACPF dipole curves does not exceed 0.06 D for the $X\,^2\Sigma^+$ state near equilibrium distance $R_e(X) \approx 1.17$ Å while the absolute value of the PDM $|d^{XX}(R_e)| \approx 1.38$ D.

[4] http://www.molpro.net

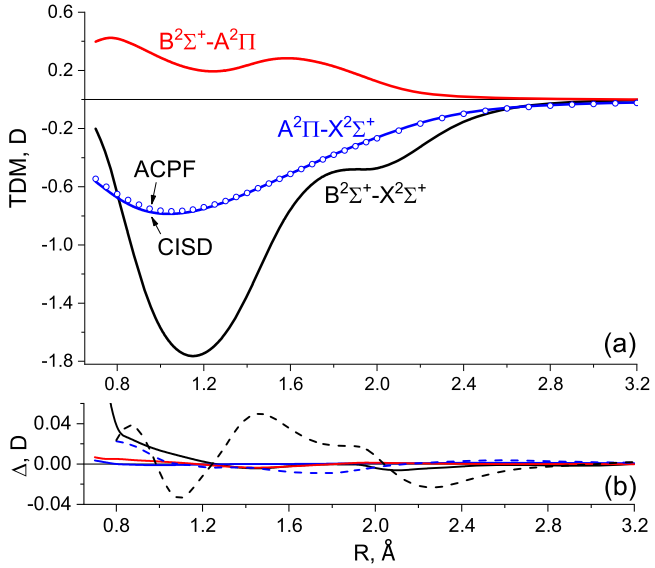

Figure 2. (a) Present *ab initio* transition dipole moment functions (in debye) obtained between the $X\,^2\Sigma^+$, $A\,^2\Pi$ and $B\,^2\Sigma^+$ states within the framework of *ic*-MR-CISD/d-aug-cc-pV5Z (solid lines) and MR-ACPF/aug-cc-pCV5Z (open circles) calculations. (b) Difference between the present *ic*-MR-CISD/d-aug-cc-pV5Z and previous *ab initio* TDM functions (dashed (J. S. A. Brooke et al. 2014) and solid (A.-M. Syme & L. K. McKemmish 2021) lines, respectively).

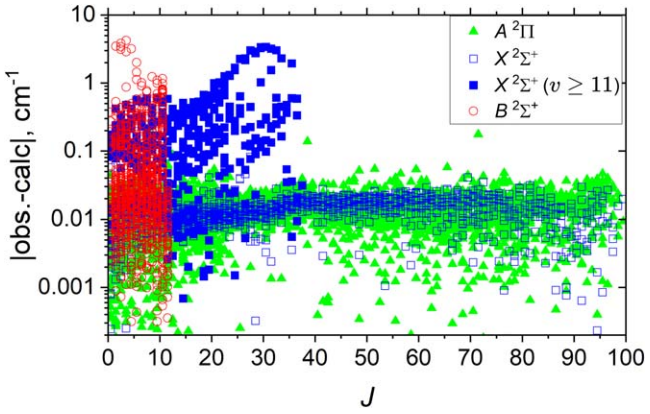

Figure 3. The absolute values of the residuals of the rovibronic energies of $^{12}C^{14}N$ as compared to the MARVEL energies (A.-M. Syme & L. K. McKemmish 2020): $X\,^2\Sigma^+$ (squared), $A\,^2\Pi$ (triangles), and $B\,^2\Sigma^+$ (circles). The filled squares indicate $X\,^2\Sigma^+$ with high vibrational excitations $v_X \geqslant 11$.

Table 1
Distribution of Vibrational Levels of the $B \sim A \sim X$ Complex Covered by the Different Sets of the Molecular Structure Parameters Taken from V. A. Terashkevich et al. (2022)

Set I	Set II	Set III
$v_X \in [0, 12]$	$v_X \in [13, 18]$	$v_X \geqslant 19$
$v_A \in [0, 16]$	$v_A \in [17, 22]$	$v_A \geqslant 23$
$v_B \in [0, 10]$	$v_B \in [11, 12]$	$v_B \geqslant 13$
$\sigma = 0.05$	$\sigma = 0.9$	$\sigma = 1.3$

Note. σ (in cm^{-1}) are conservative estimates of uncertainty in the calculated eigenvalues.

As the MR-ACPF procedure was not properly converged for the excited $B\,^2\Sigma^+$ state, all final calculations of the Einstein A_{ij} coefficients were performed using the *ic*-MR-CI/d-aug-cc-pV5Z electronic curves which are available for all the states of interest.

Important differences between our *ic*-MR-CI/d-aug-cc-pV5Z and the previous (J. S. A. Brooke et al. 2014; A.-M. Syme & L. K. McKemmish 2021) *ab initio* PDM curves are shown on Figure 1(b). The largest deviation ($\approx$0.044 D at $R = 1.4$ Å) is observed for the d^{XX} evaluated by J. S. A. Brooke et al. (2014). We note that other previous *ab initio* results (P. J. Knowles et al. 1988; S. R. Langhoff & C. W. J. Bauschlicher 1989; D. Ajitha & K. Hirao 2001) agree with the present PDM functions within a few percent.

The insets in Figure 1(a) demonstrate the reliability of the present PDM curves when compared with their experimental counterparts (R. Thomson & F. W. Dalby 1968), being -1.45 (0.08) D and $+1.15$(0.08) D for $X\,^2\Sigma^+$ and $B\,^2\Sigma^+$ states, respectively. The PDM value measured for the $A\,^2\Pi(v = 1)$ vibronic level is $+0.06$(0.02) D (M. L. Hause et al. 2009), while the present CISD estimate at the point $R = 1.24$ Å yields $d^{AA} \approx +0.11$ D.

The resulting MR-CISD CN $B\,^2\Sigma^+ - X\,^2\Sigma^+$, $A\,^2\Pi - X\,^2\Sigma^+$, and $B\,^2\Sigma^+ - A\,^2\Pi$ TDM curves are presented in Figure 2(a). For the $A - X$ transition the corresponding $d^{AX}(R)$ function was obtained within of the MR-ACPF method as well. The absolute magnitude of the present TDM functions agree within a few percent with the majority of the previous *ab initio* counterparts (C. W. J. Bauschlicher et al. 1988; P. J. Knowles et al. 1988; J. S. A. Brooke et al. 2014; A.-M. Syme & L. K. McKemmish 2021) (see, for example, Figure 2(b)). It should, however, be noted that the relative sign of the current $d^{BA}(R)$ function (in the present case, positive) exactly coincides only with a sign of the TDM derived by A.-M. Syme & L. K. McKemmish (2021), where the corresponding signs of spin–orbit and *L*-uncoupling off-diagonal electronic matrix elements are all self-consistent with signs of those evaluated by V. A. Terashkevich et al. (2021).

3.2. Einstein A Coefficients and Line Lists

The present *ic*-MR-CISD/d-aug-cc-pV5Z PDM and TDM functions were then used, according to Equations (3)–(5), to calculate the Einstein A_{ij} coefficients for all spin-allowed spontaneous emission $i \to j$ transitions coming from all rovibronic levels of both *e* and *f* parities belonging to the $B \sim A \sim X$ complex of the $^{12}C^{14}N$ isotopologue with energy up to 60,000 cm^{-1} (evaluated from the minimum of the ground state) and rotational quantum numbers $J' \in [0.5, 120.5]$. The required nonadiabatic eigenvalues and multicomponent rovibrational wave functions $\Phi_i^{CC}(R)$ were obtained from the solution of the CC Equations (1) and (2) with the three sets (see Table 1) of the electronic structure parameters. These sets were obtained by V. A. Terashkevich et al. (2022) within the framework of a mass-invariant CC deperturbation analysis of the experimental MARVEL energies (A.-M. Syme & L. K. McKemmish 2020) belonging only to the main isotopologue. These empirically refined sets of structure parameters cover the energy region and *J*-values of the $B \sim A \sim X$ complex up to 60,000 cm^{-1} and $J \leqslant 99.5$, respectively, allowing the model to reproduce the vast majority of the experimental rovibronic energies of both locally and regularly perturbed levels of the $B \sim A \sim X$ complex with almost experimental accuracy. This is illustrated in Figure 3, where we show absolute values of the observed – calculated residuals of the rovibronic energies of $^{12}C^{14}N$ as compared to the

MARVEL energies (A.-M. Syme & L. K. McKemmish 2020). The residuals show remarkably high fidelity of the majority of the energies with almost no J dependence. The largest residuals are from particular vibrational levels of the B and X states and may reflect the underlying quality of the experimental assignment or require interactions with quartet electronic states to be taken into account in the spectroscopic model.

Similarly, line lists (wavenumbers and Einstein A coefficients) were generated for the minor isotopologues $^{13}C^{14}N$, $^{12}C^{15}N$ and $^{13}C^{15}N$ that, along with the line list for $^{12}C^{14}N$, were constructed using the ExoMol format (J. Tennyson et al. 2020) consisting of a States file and Transition file. Following A.-M. Syme & L. K. McKemmish (2020), we used the experimentally derived MARVEL energies of $^{12}C^{14}N$ by A.-M. Syme & L. K. McKemmish (2020) to replace the theoretical values in the States file of $^{12}C^{14}N$ in the MARVELized approach. Unlike A.-M. Syme & L. K. McKemmish (2020), however, we did not incorporate the effective Hamiltonian MoLLIST values from J. S. A. Brooke et al. (2014). We believe that the quality of our calculated energies should be comparable or in cases of perturbations even better than that of the MoLLIST values.

An ExoMol State file contains state IDs, energy term values, state degeneracies, uncertainties, radiative lifetimes, magnetic g-factors, and quantum numbers. In Table 2, an extract of the States file of $^{12}C^{14}N$ is given as an illustration of the format. The Transition files contain upper and lower IDs, Einstein A coefficients, and transition frequency wavenumbers. As part of the ExoMol data set, partition functions of the three isotopologues on the temperature range from 0 to 10,000 K are provided as generated using the new line lists using the standard Boltzmann summation.

Figure 4 gives an overview of the line list, which we call KTPSYT, for the parent isotopologue in the form of an absorption spectrum at $T = 3000$ K, where the three main bands $B\,^2\Sigma^+ - X\,^2\Sigma^+$, $A\,^2\Pi - X\,^2\Sigma^+$, and $X\,^2\Sigma^+ - X\,^2\Sigma^+$ are indicated. The figure also shows the differences between KTPSYT and the two previous CN line lists, MoLLIST and TriHybrid, as taken from the ExoMol database. It should be noted that because KTPSYT and TriHybrid have been MARVELized (i.e., replaced with experimentally derived energies) using the same MARVEL set (A.-M. Syme & L. K. McKemmish 2020), the corresponding line positions connecting these states should be identical in these two line lists, but only for the MARVELized transitions. The intensities are based on different dipole moments and also different wave functions, and are therefore important to compare. The profiles of the $X - X$ and $A - X$ bands appear to agree very well across all three line list, while the $B - X$ bands show larger differences. This point is discussed in detail below.

Figure 5 illustrates the completeness of the line list by showing the integrated absorption of $^{12}C^{14}N$ for the range from 0 to 40,000 cm^{-1} as a function of temperature. There is a small drop in the completeness at high temperatures. This figure also shows the completeness of the MARVELized part of the line list. Despite a larger drop in the total intensities, the MARVElized data provides a fairly complete description of the absorption. To put this more quantitatively, at $T = 4000$ K, there are 992,804 transitions in the $^{12}C^{14}N$ line list with the intensities larger than 10^{-25} cm/molecule in total, 235,447 of which (i.e., about one-quarter) are MARVELized.

3.3. Oscillator Strengths

The Einstein A coefficients calculated above were employed, according to Equation (6), to evaluate oscillator strengths f_{ij} for the lower rotational lines of the $X\,^2\Sigma^+(\upsilon_X = 0) \rightarrow B\,^2\Sigma^+(\upsilon_B = 0)$ transition, which are used by the astrophysical community, in conjunction with the corresponding wavenumbers ν_{ij} and relative intensity measurements, to assess the temperature of the cosmic microwave background radiation, T_{CMBR}, from interstellar CN absorption (see Table 3). In contrast to the previous compilation by K. C. Roth et al. (1993), our f-values explicitly take into accounted the fine structure (γ-splitting) of the upper and ground $^2\Sigma^+$ states as well as regular perturbations of the upper and lower states within of the framework of the $B \sim A \sim X$ complex considered. Thus, for the indicated rovibronic transition, up to six rotational branches should be explicitly observable in a high-resolution astronomical spectra of CN.

3.4. Radiative Lifetimes and Vibronic Branching Ratios

Our calculated Einstein A coefficients, A_{ij}, were used in Equation (8) to estimate radiative lifetimes τ_i for all rovibronic stats, i, of the excited $A\,^2\Pi$ and $B\,^2\Sigma^+$ as well as ground $X\,^2\Sigma^+$ electronic states. τ_i values derived for the lowest vibrational levels of the A and B states are presented in Tables 4 and 5, respectively, where they are compared with their experimental and previous theoretical counterparts. These $\tau_i^{\text{Calc.}}$ values correspond to the lowest $J(N)$ values and they are averaged over the e/f levels. The $\tau_A^{\text{Calc.}}$ values in Table 4 were additionally averaged over the $A\,^2\Pi_{1/2}$ and $A\,^2\Pi_{3/2}$ spin–orbit splitting components.

The overall τ_A and τ_B values depend smoothly on the e/f parity and the upper-level quantum numbers except for cases of strong local perturbations. Considering the trend in lifetimes, there is general agreement between the experimental and the calculated values: for the long-living (metastable) A-state the $\tau_A^{\text{Calc.}}$ values rapidly decrease as the υ_A values increase, while $\tau_B^{\text{Calc.}}$ values slowly increase as υ_B increases. The $\tau_A^{\text{Calc.}}$ values for the lowest vibrational levels show a pronounced increase with rotational excitation which can be attributed to the strong "nondiagonal" character of the $A - X$ electronic transition.

The radiative lifetimes evaluated for the perturbed rotational $N_B = 4$ and seven levels of the $B\,^2\Sigma^+(\upsilon_B = 0)$ state are presented in Table 6. The pronounced local perturbations in the experimental term values of these particular levels as well as their lifetimes were discovered in early works (W. M. Jackson 1974; N. Duric et al. 1978). The present deperturbation treatment correctly reproduces both positions of observed levels (see the calculated fractional population of $B\,^2\Sigma^+$ state) and their radiative properties.

Table 7 contains branching ratios R_{ijk} evaluated using Equation (7) for $B - A(0, 0)/B - X(0, 1)$, and $B - X(0, 2)/B - X(0, 1)$ vibronic transitions started from the $N_B = 5$ rotational level of the $B\,^2\Sigma^+(\upsilon_B = 0)$ state. The present $R_{ijk}^{\text{Calc.}}$ values are found to be in excellent agreement with the experimental data of M. Costes et al. (1985). The Einstein A coefficient calculated for the $B - A(0, 0)$ band in the present work is $6.56 \times 10^4\ s^{-1}$, which also agrees well with its the experimental counterparts 7.4(4.1) (J. B. Halpern & X. Tang 1983) and 5(2) (M. Costes et al. 1985).

Table 2
Extract from the KTPSYT

i	$\tilde{E}$ (cm^{-1})	g_i	J	Unc. (cm^{-1})	τ (s^{-1})	g	Parity		State	v	Λ	Σ	Ω	Ma/Ca	$\tilde{E}$ (cm^{-1})
2940	58,674.021391	48	7.5	1.300000	5.8075e-06	−0.045648	−	e	A	39	−1	0.5	−0.5	Ca	58,674.021391
2941	58,892.762437	48	7.5	1.300000	3.8102e-04	0.133474	−	e	X	39	0	−0.5	−0.5	Ca	58,892.762437
3001	136.083884	48	7.5	0.001374	1.4089e+02	−0.117782	+	f	X	0	0	0.5	0.5	Ma	136.092855
3002	2177.252041	48	7.5	0.000728	9.1465e-02	−0.117782	+	f	X	1	0	0.5	0.5	Ma	2177.258199
3003	4192.121972	48	7.5	0.001540	4.5697e-02	−0.117782	+	f	X	2	0	0.5	0.5	Ma	4192.128321
3004	6180.656303	48	7.5	0.001784	3.0495e-02	−0.117782	+	f	X	3	0	0.5	0.5	Ma	6180.663636
3005	8142.812014	48	7.5	0.001794	2.2931e-02	−0.117782	+	f	X	4	0	0.5	0.5	Ma	8142.823149
3006	9193.778571	48	7.5	0.003034	1.1200e-05	0.098955	+	f	A	0	1	0.5	1.5	Ma	9193.785941
3007	9256.071794	48	7.5	0.002900	1.1021e-05	−0.051879	+	f	A	0	1	−0.5	0.5	Ma	9256.091678
3008	10,078.550590	48	7.5	0.002115	1.8402e-02	−0.117781	+	f	X	5	0	0.5	0.5	Ma	10,078.564192
3009	10,980.506070	48	7.5	0.003629	9.7123e-06	0.098626	+	f	A	1	1	0.5	1.5	Ma	10,980.518103

Note. States file. i: state counting number. e/f: rotation-less parity. $\tilde{E}$: state energy term values in cm^{-1}, MARVEL or calculated. State: electronic state. g_i: total statistical weight, equal to $g_{ns}(2J+1)$. v: state vibrational quantum number. J: total angular momentum. Λ: projection of the electronic angular momentum. Unc: uncertainty, cm^{-1}. Σ: projection of the electronic spin. τ: radiative lifetime (s^{-1}). Ω: projection of the total angular momentum, $\Omega = \Lambda + \Sigma$. g: Landé g-factors (S. V. Kozlov et al. 2024). Ma/Ca: "Ma" is for MARVEL and "Ca" is for calculated. $+/-$: total parity. $\tilde{E}$: state energy term values in cm^{-1}, calculated.

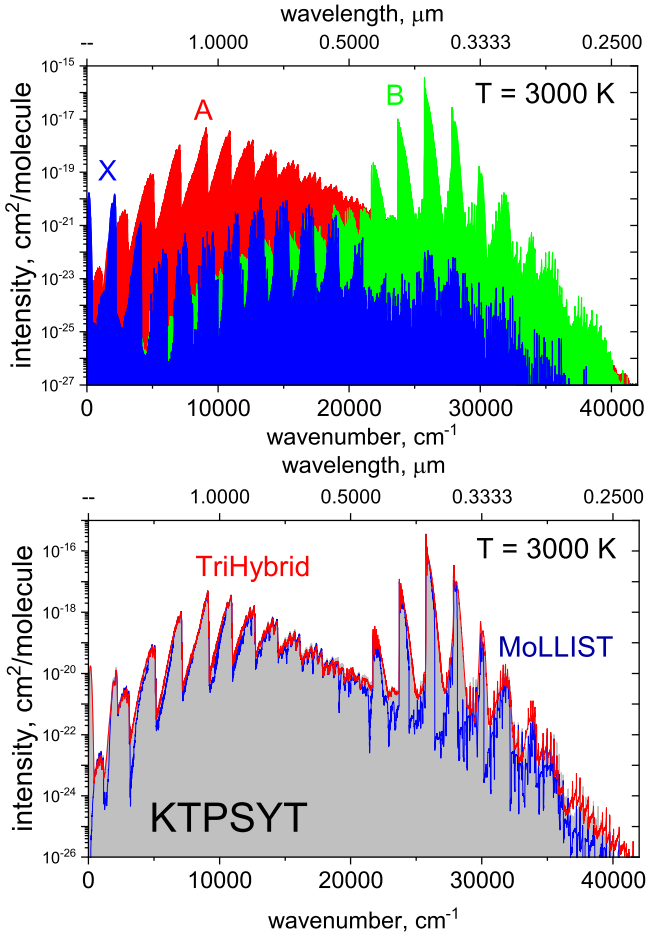

Figure 4. Overview of the band structure of the CN absorption spectrum computed using the KTPSYT line list with the ExoCross program compared to other line lists for CN, TriHybrid, and MoLLIST. A temperature of $T = 3000$ K is used with a Gaussian line profile of HMHM = 1 cm^{-1}.

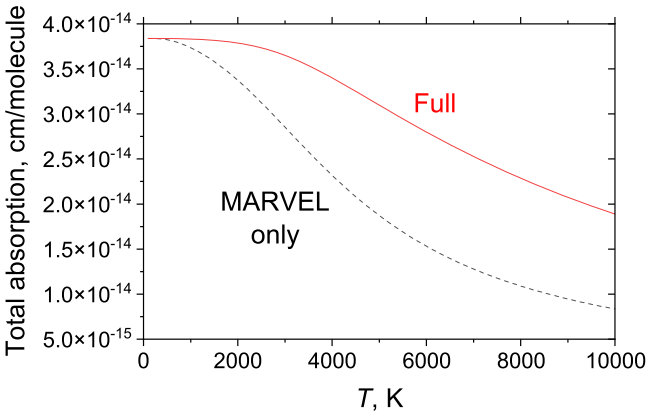

Figure 5. Completeness of the line lists: integrated intensity (ν = [0…40,000] cm^{-1}) vs temperature of the line list for $^{12}C^{14}N$: solid line indicates values obtained using the full line list while the dashed line is for the MARVELized transitions only.

3.5. Intensity Distribution in the Locally Perturbed Lines

Among the radiative properties considered for the $B \sim A \sim X$ complex, the intensity distributions in rotationally resolved spectra corresponding to the strongly "nondiagonal" $A - X$ and $B - A$ electronic transitions seem (N. Furio et al. 1989) to be the most sensitive to *local* spin–orbit and Coriolis perturbations

Table 3
Experimental Wavenumbers (A. -M. Syme & L. K. McKemmish 2020) ν, in cm^{-1}, and Theoretical Oscillator Strengths f Corresponding to the Low-lying Rotational Lines of the $X\,^2\Sigma^+ \rightarrow B\,^2\Sigma^+(0, 0)$ Absorption Band of the $^{12}C^{14}N$ Isotopologue

Rotational Line	ν (MARVEL)	$\Delta\nu$	$f \times 10^{-2}$ (PW)	(TriHybrid)	(1)
$R_1(0)$	25,801.777	−0.014	2.308	2.195	3.42
$Q_{21}(0)$	25,801.770	0.003	1.150	1.099	
$R_1(1)$	25,805.845	−0.003	2.078	1.975	2.28
$R_2(1)$	25,805.824	0.007	2.303	2.197	
$Q_{21}(1)$	25,805.820	0.014	0.230	0.220	
$P_1(1)$	25,794.091	0.011	1.150	1.099	1.14
$Q_{12}(1)$	25,794.095	0.004	1.154	1.097	
$R_1(2)$	25,810.037	−0.003	1.980	1.881	2.05
$R_2(2)$	25,810.005	0.006	2.073	1.976	
$Q_{21}(2)$	25,810.000	0.019	0.098	0.094	
$P_1(2)$	25,790.433	−0.005	1.380	1.318	1.37
$P_2(2)$	25,790.430	−0.001	1.153	1.098	
$Q_{12}(2)$	25,790.438	−0.018	0.231	0.219	

Note. $\Delta\nu$ is the residual of the MARVEL wavenumbers (A.-M. Syme & L. K. McKemmish 2020) from their theoretical counterparts evaluated by V. A. Terashkevich et al. (2022). The values in brackets are the rotational quantum number N'' of the ground state. Both ν and $\Delta\nu$ values are given in cm^{-1}, while f-values are dimensionless. (TriHybrid) A.-M. Syme & L. K. McKemmish (2021); (1) K. C. Roth et al. (1993).

Table 4
Radiative Lifetimes (in Microseconds) Calculated for the Lower Vibrational Levels of the $A\,^2\Pi$ State as Well as Their Experimental $\tau_A^{\text{Exp.}}$ and Theoretical $\tau_A^{\text{Calc.}}$ Counterparts

υ_A	$\tau_A^{\text{Exp.}}$ (1)	(2)	$\tau_A^{\text{Calc.}}$ (3)	(4)	(5)	(PW)
0	14.2	⋯	10.8	10.9	11.2	11.1
1	11.6	⋯	9.5	9.5	9.7	9.6
2	10.2	3.83(0.5)	8.6	8.4	8.6	8.6
3	9.0	4.05(0.4)	7.9	7.6	7.8	7.8
4	8.0	3.98(0.4)	7.3	7.0	7.2	7.1
5	7.4	4.20(0.4)	6.8	6.6	6.7	6.7
6	6.8	4.35(0.4)	6.5	6.2	6.3	6.3
7	6.3	4.35(0.4)	6.2	5.9	5.9	6.0
8	5.9	4.50(0.4)	6.0	5.6	5.7	5.8
9	5.5	4.28(0.4)	5.7	5.4	5.4	5.5
10	5.2	4.10(0.4)	5.5	5.2	5.3	5.2

Note. Experimental uncertainties are given in brackets. There are also the alternative $\tau_A^{\text{Exp.}}$ values averaged over several vibrational states, namely 5.6 μs for the $\upsilon_A \in [7, 9]$ levels (H.-S. Lin et al. 1994). (1) C. Sneden & D. L. Lambert (1982); (2) N. Duric et al. (1978) ; (3) A.-M. Syme & L. K. McKemmish (2021); (4) L. Liu & X. Cheng (2022); (5) J. S. A. Brooke et al. (2014).

in upper/lower levels of the rovibronic $B \sim A - X / B - A \sim X$ transitions, respectively. This phenomena becomes of particular importance in the case of locally perturbed lines due to the interference terms $\pm 2M_{ij}^{kl} M_{ij}^{mn}$ appearing in Equation (3) for the *parallel* $B - X$ ($\Delta\Lambda = 0$) and perpendicular $B - A$, $A - X$ ($\Delta\Lambda = \pm 1$) bands (R. Lefebvre & R. Field 2004).

To probe this assumption we have simulated relative intensity distributions in the rotational structure of the strongly perturbed $B(\upsilon_B = 8) \rightarrow A(\upsilon_A = 7) \sim X(\upsilon_X = 11)$ bands. The

Table 5
Comparison of the Experimental $\tau_B^{\text{Exp.}}$ and Calculated $\tau_B^{\text{Calc.}}$ Radiative Lifetimes (in Nanoseconds) for the Lowest Vibrational Levels of the $B\,^2\Sigma^+$ State

υ_B	$\tau_B^{\text{Exp.}}$		$\tau_B^{\text{Calc.}}$				
	(1)	(2)	(3)	(4)	(5)	(6)	(PW)
0	59.0	63.8(0.6)	60.7	62.5	62.8	62.7	60.8
1	59.4	66.3(0.8)	61.2	63.2	62.9	63.0	61.3
2	59.4	64.3(2.0)	62.0	64.2	63.2	63.5	62.0
3	64.8	65.6(3.0)	63.1	65.5	63.8	64.3	63.1
4	63.5	68.2(4.0)	65.0	67.2	64.7	65.4	64.5
5	63.2	67.3(5.0)	66.4	69.3	66.1	67.0	66.4

Note. Experimental uncertainties are given in brackets. There are also the experimental $\tau_B^{\text{Exp.}}$ values being averaged over several vibrational levels: 85 (R. G. Bennett & F. W. Dalby 1962), 60.8 (C. K. Luk & R. Bersohn 1973), 82 (J.H.J. Moore & D.W. Robinson 2003) for $\upsilon_B \in [0, 4]$, and 61.1 (K. A. Mohamed et al. 1977) for $\upsilon_B \in [0, 1]$. (1) H. S. Liszt & J. E. Hesser (1970); (2) N. Duric et al. (1978); (3) P. J. Knowles et al. (1988); (4) L. Liu & X. Cheng (2022); (5) A.-M. Syme & L. K. McKemmish (2021); (6) J. S. A. Brooke et al. (2014).

Table 6
Comparison of Measured $\tau_B^{\text{Exp.}}$ (Uncertainties are Given in Brackets) and Calculated $\tau_B^{\text{Calc.}}$ Lifetimes (in Nanoseconds) for the Rotational N_B Levels of the $B\,^2\Sigma^+$ ($\upsilon_B = 0$) State Perturbed by the Nearby $A\,^2\Pi$ ($\upsilon_A = 10$) State

N_B	$\tau_B^{\text{Exp.}}$		$\tau_B^{\text{Calc.}}(e/f)$		$P_B(e/f)$
	(1)	(2)	(3)	(PW)	(PW)
0	66.7(1.4)	65.1(0.8)	62.8/⋯	60.8/⋯	100/⋯
1	64.8(1.4)	66.9(0.5)	62.8/62.8	60.8/60.8	100/100
2	65.8(1.4)	64.8(0.6)	62.8/62.8	60.8/60.8	100/100
3	68.0(1.4)	65.0(0.6)	62.8/62.8	60.8/60.8	100/100
4*	72.9(0.6)	71.1(0.3)	62.8/77.7	60.8/71.5	100/85
5	66.7(0.6)	67.4(0.4)	62.8/62.8	60.8/60.8	100/100
6	66.5(0.8)	64.2(0.7)	63.0/62.8	60.9/60.8	100/100
7*	68.2(0.8)	67.0(0.7)	77.5/62.8	69.9/60.8	87/100
8	64.6(0.6)	65.7(0.8)	63.3/62.8	61.0/60.8	100/100
9	65.1(0.7)	66.4(0.5)	62.9/62.8	60.8/60.7	100/100
10	65.6(0.7)	64.9(0.3)	62.8/62.9	60.8/60.7	100/100
11*	66.3(0.7)	66.0(0.4)	62.7/76.7	60.8/61.3	100/99
12	65.6(0.7)	64.9(0.4)	62.7/63.0	60.7/60.7	100/100
13	69.2(0.8)	65.6(0.4)	62.7/62.8	60.7/60.7	100/100
14	69.7(0.8)	64.0(0.3)	62.7/62.7	60.8/60.7	100/100
15*	65.3(0.7)	⋯	83.3/62.7	77.0/60.7	79/100
16	63.4(0.5)	⋯	62.7/62.6	60.8/60.7	100/100

Note. The symbol * marks the locally perturbed levels of the B-state. The experimental lifetimes were not distinguished for the e/f components. $P_B = \langle \phi_B | \phi_B \rangle$ is the fractional population (in percent) of the B-state levels calculated by Equation (2). (1) N. Duric et al. (1978); (2) W. M. Jackson (1974); (3) A.-M. Syme & L. K. McKemmish (2021).

Table 7
Comparison of the Branching Ratios R_{ijk} Evaluated for $B - A$ and $B - X$ Bands with Their Previous Experimental and Theoretical Counterparts

Branching Ratios	$R_{ijk}^{\text{Exp.}}$	$R_{ijk}^{\text{Calc.}}$	
	(1)	(2)	(PW)
$B - A(0, 0)/B - X(0, 1)$	0.054(0.011)	0.061	0.052
$B - X(0, 2)/B - X(0, 1)$	0.047(0.009)	0.059	0.047

Note. Uncertainties for experimental values are given in brackets. (1) M. Costes et al. (1985); (2) A.-M. Syme & L. K. McKemmish (2021).

Table 8
Fractional Populations, P_i (in Percent), Calculated for the Mutual Perturbed $B\,^2\Sigma^+(\upsilon_B = 5)$ and $A\,^2\Pi$ ($\upsilon_A = 17$) Terms for the Rotational Level $J = 12.5$ of $^{12}C^{14}N$ Isotopologue

Line	P_B	$P_{A_{1/2}}$	$P_{A_{3/2}}$
$R_1(11.5)$	55.4	38.4	6.2
$R_{21}(11.5)$	44.1	52.5	3.4

good agreement of the relative intensity distributions in the stick spectra simulated for emission lines in the overlapping $B\,^2\Sigma^+ - A\,^2\Pi(8, 7)$ and $B\,^2\Sigma^+ - X\,^2\Sigma^+(8, 11)$ bands (see Figure 6) with the fragment of the original experimental spectra depicted in Figure 3(a) of N. Furio et al. (1989) proves the correctness of both the relative sign and absolute magnitude of the present *ab initio* $d^{BA}(R)$, $d^{BX}(R)$ TDM functions. At the same time, the vibrationally averaged ratio $M^{BX}/M^{BA} = +2.96$ predicted for the $B - X(8, 11)/B - A(8, 7)$ vibronic transitions is approximately $\sqrt{2}$ times larger than its experimental counterpart $+2.0(0.2)$ derived by N. Furio et al. (1989). Presumably the source of this discrepancy can be attributed to an improper normalization factor applied by N. Furio et al. (1989) to the Hönl–London factors of the perpendicular $\Sigma - \Pi$ transitions (J. K. G. Watson 2008).

Strong mutual perturbations between the nearby $B\,^2\Sigma^+(\upsilon_B = 5)$ and $A\,^2\Pi(\upsilon_A = 17)$ vibronic terms of the $^{12}C^{14}N$ isotopologue are experimentally established for the region of the rotational quantum numbers $J \in [9.5, 12.5]$ (R. S. Ram et al. 2010). These local perturbations particularly lead to line shifts and irregular distribution of intensities in the $B\,^2\Sigma^+(\upsilon_B = 5) \rightarrow X\,^2\Sigma^+(\upsilon_X = 4)$ emission bands, for which experimental line positions and their intensities are available. Figure 7 demonstrates the modeling $B \sim A(\upsilon_B = 5 \sim \upsilon_A = 17) \rightarrow X(\upsilon_X = 4)$ spectra obtained using program ExoCross (S. N. Yurchenko et al. 2018) together with its experimental counterpart taken from R. Engleman (1974). Overall good agreement between synthetic and experimental spectra is observed. Furthermore, the present deperturbation treatment (see Table 8) allowed us to reassigned the satellite $R_{21}(11.5)$ line to the nominally "dark" $A\,^2\Pi - X\,^2\Sigma^+(17,4)$ transition.

3.6. Intensity Distributions in Laser-induced Plasma Spectra

Figure 8 displays a fragment of the high-temperature $B\,^2\Sigma^+ \rightarrow X\,^2\Sigma^+$ emission spectra recorded for the diagonal ($\upsilon_B = \upsilon_X$) band system of $^{12}C^{14}N$ during the LIBS of a carbon-containing target in air (C. G. Parigger et al. 2015). The original experimental spectrum is compared with its theoretical counterparts simulated using ExoCross (S. N. Yurchenko et al. 2018) and each of the available line lists, namely MoLLIST (J. S. A. Brooke et al. 2014), TriHybrid (A.-M. Syme & L. K. McKemmish 2021), and our present one.

It should be remembered that the diagonal $B - X$ system of CN is characterized by overlapping rovibronic transitions corresponding to highly excited rotational levels of the (0, 0) band with lines belonging to higher excited vibrational bands. Similarly, the higher rotational transitions of the (1, 1) band contribute to the intensity of the (2, 2) band, and so on. Band heads leading to the reversal of rovibronic transitions from the region with high wavenumbers to lower ones with increasing of rotational quantum numbers are observed for this system. Therefore, an accurate line list becomes particularly important

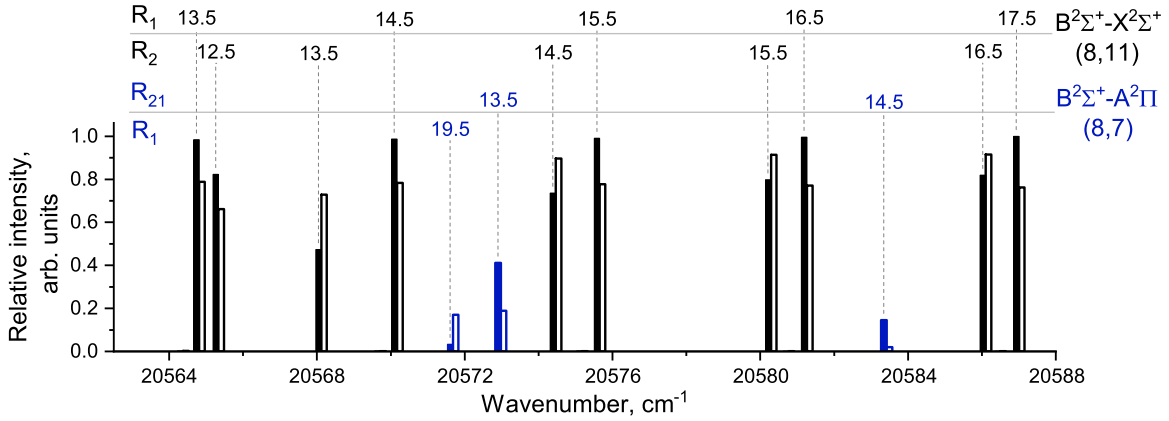

Figure 6. Relative intensity distribution in the rovibronic transitions calculated in the overlapping $B\,^2\Sigma^+ - A\,^2\Pi(8,\,7)$ and $B\,^2\Sigma^+ - X\,^2\Sigma^+(8,\,11)$ bands with an alternative sign of the $d^{BA}(R)$ TDM function: filled columns correspond to original (plus) sign (see Figure 2), empty columns to the opposite (minus) sign.

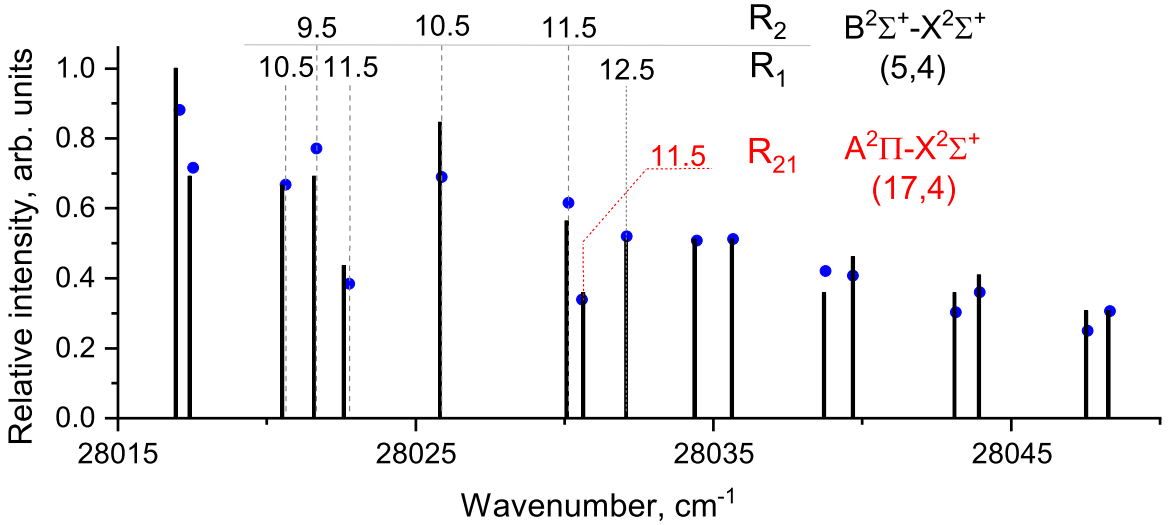

Figure 7. Comparison of a fragment of the $B\,^2\Sigma^+ \rightarrow X\,^2\Sigma^+(5,\,4)$ band simulated in the perturbation region of the $A\,^2\Pi(\upsilon_A = 17)$ state with the experimental stick spectra obtained during the flash photolysis of a BrCN molecule by R. Engleman (1974). The highlighted $R_{21}(11.5)$ line has been reassigned to the satellite $A\,^2\Pi - X\,^2\Sigma^+(17,\,4)$ transition.

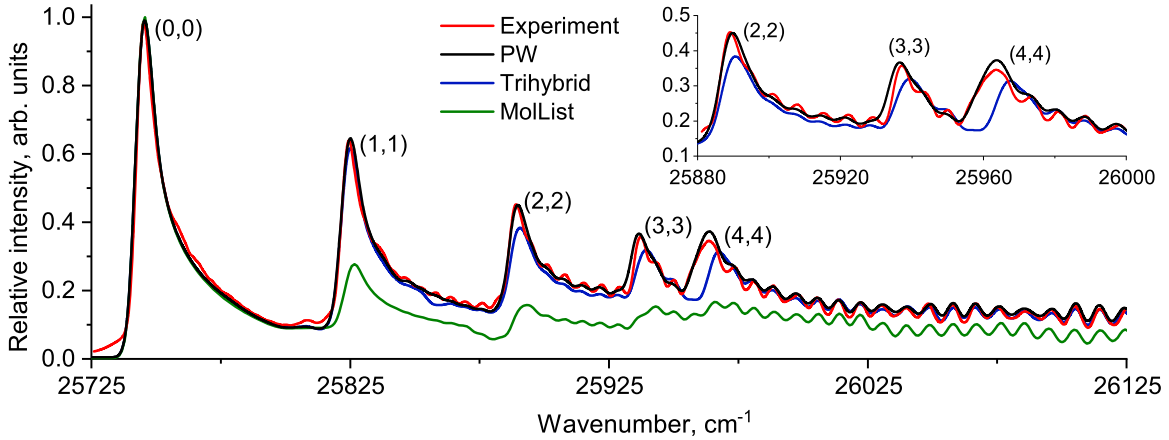

Figure 8. Comparison of high-temperature experimental and simulated emission spectra for the diagonal $\upsilon_B = \upsilon_X\, B\,^2\Sigma^+ \rightarrow X\,^2\Sigma^+(\upsilon_B,\upsilon_X)$ bands of the $^{12}C^{14}N$ radical. The model spectra were reconstructed using ExoCross (S. N. Yurchenko et al. 2018) and the TriHybrid (A.-M. Syme & L. K. McKemmish 2021), MoLLIST (J. S. A. Brooke et al. 2014), and our KTPSYT rovibronic line lists. The distributions of relative intensities are normalized to the intensity of the (0, 0) band head. The experimental LIBS spectra were taken from the supplementary file of C. G. Parigger et al. (2015). The ExoCross simulations used LTE with a rovibrational temperature $T = 6840$ K and Gaussian line profiles with HWHM of 3.2 cm^{-1} corresponding to the spectral resolution (FWHM) = 0.093 nm at $\lambda = 380$ nm as in C. G. Parigger et al. (2015) (see caption to Figure B.2 there).

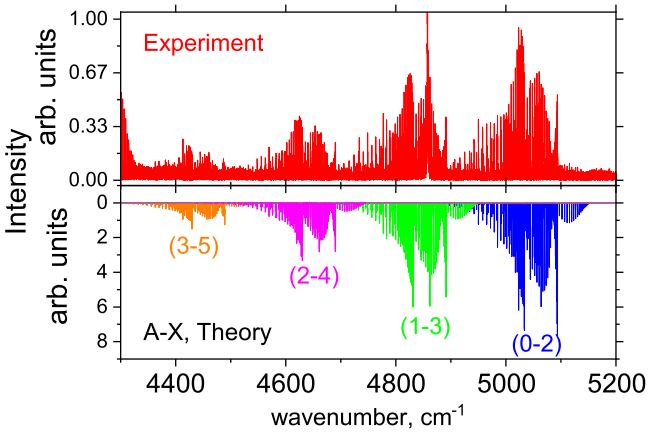

Figure 9. Lower panel: non-LTE emission spectrum of $^{12}C^{14}N$ ($T_{rot} = 300$ K and $T_{vib} = 4000$ K) computed using the KTPSYT line list for $^{12}C^{14}N$ with a Voigt profile of HWHM = 0.012 cm^{-1}. Upper panel: experimental spectrum of CN by M. Ferus et al. (2011).

for high rotational levels for the correct representation of even rotationally unresolved spectra.

The divergence of the experiment from the MoLLIST model spectra in Figure 8 is already visible in the (1, 1) band. For the following (2, 2), (3, 3), and (4, 4) bands the intensities evaluated with the TriHybrid line list are also underestimated alongside some deviation in the overlapping line positions, which is especially noticeable for the highest identified band, the (4, 4) band. The MoLLIST data reproduces the energetic and radiative properties of transitions limited to low rotational excitation quite well, but underestimates the intensities beginning with the (1, 1) band. In contrast, our KTPSYT line list demonstrates overall good agreement with the high-temperature spectra: the relative intensity distributions are reproduced correctly over the entire wavenumber range. The marked deviation between the present and TriHybrid spectra can be attributed to the fact that even the narrow spectral region (for instance, 2–4 cm^{-1} located near the (4, 4) band head) can indeed contain rovibronic transitions from different regions of rotational and vibrational quantum numbers and, hence, be characterized by the quite different intensity contributions of the particular transitions.

3.7. A–X *System: Non-LTE Spectral Simulations*

As an illustration of the applicability of our *A–X* line list to high-temperature environments, Figure 9 simulates a non-LTE emission spectrum of four hot bands of $^{12}C^{14}N$ using KTPSYT at $T_{rot} = 300$ K and $T_{vib} = 4000$ K and compares it to the experimental spectrum of CN by M. Ferus et al. (2011). Here, a Voigt profile was used, with a half-width at half-maximum (HWHM) of 0.012 cm^{-1}. The latter was recorded as part of a time-resolved Fourier transform study of formamide ($HCONH_2$) in pulsed-glow discharges. Due to the non-LTE conditions, the CN molecules are found with highly excited vibrational excitations, reproduced well in our simulations even with our very simplistic two-temperature non-LTE model. A more sophisticated non-LTE model would be required for a more quantitative description of the experiment, which is beyond the goals of this study.

3.8. A–X *System: Modeling Stellar Spectra of CN*

As an illustration of possible astrophysical applications of KTPSYT, Figure 10 compares spectra of the carbon star HD 92055, observed at low resolution ($R = 2500$) by J. T. Rayner et al. (2009) and at high resolution ($R = 80{,}000$) by S. Bagnulo et al. (2003), to a simple model of transmittance of $^{12}C^{14}N$ in this region corresponding to the *A–X* system typical for this type of object. Our absorption cross sections of CN are computed at $T = 3500$ K with a Gaussian line profile with HWHM of 0.23 cm^{-1}. The vacuum-to-air conversion is as by D. C. Morton (2000). The radial velocity of the star of 23.5 km and the number density of 7×10^{17} cm^{-3} was assumed. Even without proper radiative transfer simulations of the stellar atmosphere, which would be required for a more quantitative analysis of these systems (beyond our current goals), both the general band structure and line positions are well reproduced. Together with the illustration of the quality of our intensities in Figure 9, this is a good example of how KTPSYT can be useful in stellar analyses.

4. Concluding Remarks

The mass-invariant CC deperturbation model of V. A. Terashkevich et al. (2022) has been systematically utilized to generate line lists for radiative transitions between the mutually perturbed rovibronic levels belonging to the $B \sim A \sim X$ complex of the CN radical.

The permanent and transition dipole moments between states of the complex were reevaluated within the *ab initio* frameworks of the MR-CI and of the MR-ACPF methods combined with all electrons' *aug-cc-pCVnZ* ($n = 5$, 6) basis sets. Both *ab initio* PDM and TDM curves showed good convergence with the respect to atomic basis expansion. The observed small divergence of the MR-CISD and MR-ACPF results can be attributed to the residual electron-correlation error.

Our revised oscillator strengths for the low-lying rotational transitions within the $X\,^2\Sigma^+ \rightarrow B\,^2\Sigma^+(0, 0)$ absorption band are recommended for use in alternative determinations of the temperature of the cosmic microwave background radiation by means of accurate processing (deconvolution) of the relevant interstellar lines recorded with full and/or partly resolved Λ-doubling structure (K. Słyk et al. 2008; S. Leach 2012).

As expected, our computed radiative lifetimes for the excited $A\,^2\Pi$ and $B\,^2\Sigma^+$ states overall show a smooth dependence on the e/f parity and rotational and vibrational quantum numbers of the upper levels except for rare cases of strong local perturbations. Our calculated vibronic state lifetime, $\tau_i^{Calc.}$, agrees within a few percent with the most previous theoretical counterparts. Despite several sets of measured lifetimes, it is not possible to provide a definitive set of experimental values due to the large scatter in the measurements; however, our calculated lifetimes are in agreement with a subset of the measured values.

Since the present line list provides very good agreement with the experimental line positions and intensities of locally perturbed and highly excited rotational lines, we believe that our line lists can be particularly useful for modeling optical spectra of the CN isotopologues over a wide temperature range, including both cold interstellar clouds and high-temperature laser-induced plasma.

The KTPSYT line lists containing energies, statistic weights, radiative lifetimes, and Landé *g*-factors for rovibrotinal levels of the $X\,^2\Sigma^+$, $A\,^2\Pi$, and $B\,^2\Sigma$ states of the $^{12}C^{14}N$, $^{13}C^{14}N$,

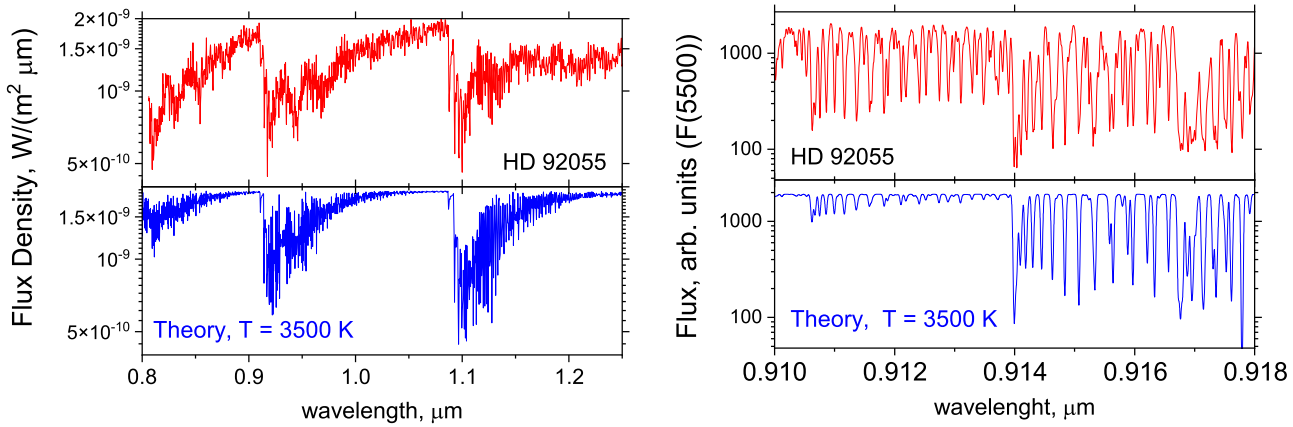

Figure 10. Spectrum of the carbon star HD 92055 compared to the cross sections from this work: Upper panels: low-(J. T. Rayner et al. 2009) and high- (S. Bagnulo et al. 2003) resolution observed spectra. Lower panels: simulated transmittance spectra calculated using the KTPSYT line list for $T = 3500$ K and a Gaussian line profile of HWHM = 0.23 cm^{-1}, assuming a radial velocity of the star of 23.5 km and a number density of 7×10^{17} cm^{-3}.

^{12}C^{15}N, and ^{13}C^{15}N isotopologues (.states files) as well as the corresponding rovibronic transition wavenumbers and Einstein A coefficients (.trans files) in ExoMol format can be found at www.exomol.com.

Acknowledgments

This work was supported by the Russian Science Foundation (RSF) grant No.23-13-00207, the European Research Council (ERC) under the European Union's Horizon 2020 research and innovation program through Advance grant No. 883830 and the STFC Project No. ST/Y001508/1.

Appendix
Supplementary Materials

The supplementary .tar.gz archive contains the present *ab initio* point-wise PDM and TDM functions as well as three sets of potential energy curves and nonadiabatic coupling functions required to evaluate eigenvalues and eigenfunctions of the $B \sim A \sim X$ complex of CN according to the CC deperturbation model of V. A. Terashkevich et al. (2022).

ORCID iDs

S. V. Kozlov https://orcid.org/0000-0002-3619-5554
V. A. Terashkevich https://orcid.org/0000-0003-3844-3811
E. A. Pazyuk https://orcid.org/0000-0003-0568-7801
A. V. Stolyarov https://orcid.org/0000-0001-7046-7202
S. N. Yurchenko https://orcid.org/0000-0001-9286-9501
J. Tennyson https://orcid.org/0000-0002-4994-5238

References

Ajitha, D., & Hirao, K. 2001, CPL, 347, 121
Bagnulo, S., Jehin, E., Ledoux, C., et al. 2003, Msngr, 114, 10
Bauschlicher, C. W. J., Langhoff, S. R., & Taylor, P. R. 1988, ApJ, 332, 531
Bennett, R. G., & Dalby, F. W. 1962, JChPh, 36, 399
Bernath, P. F. 2020, JQSRT, 240, 106687
Bose, D., Wright, M. J., Bogdanoff, D. W., Raiche, G. A., & Allen, G. A. 2006, JTHT, 20, 220
Brooke, J. S. A., Ram, R. S., Western, C. M., et al. 2014, ApJS, 210, 23
Brown, J. M., Colbourn, E. A., Watson, J. K. G., & Wayne, F. D. 1979, JMoSp, 74, 294
Costes, M., Naulin, C., & Dorthe, G. 1985, CPL, 113, 569
Duric, N., Erman, P., & Larsson, M. 1978, PhyS, 18, 39
Engleman, R. 1974, JMoSp, 49, 106
Federman, S. R., Danks, A. C., & Lambert, D. L. 1984, ApJ, 287, 219
Ferus, M., Kubelík, P., Kawaguchi, K., et al. 2011, JPCA, 115, 1885
Fray, N., Bénilan, Y., Cottin, H., Gazeau, M.-C., & Crovisier, J. 2005, P&SS, 53, 1243
Furio, N., Ali, A., Dagdigian, P. J., & Werner, H.-J. 1989, JMoSp, 134, 199
Gordon, I. E., Rothman, L. S., Hargreaves, R. J., et al. 2022, JQSRT, 277, 107949
Halpern, J. B., & Tang, X. 1983, CPL, 97, 170
Hänni, N., Altwegg, K., Pestoni, B., et al. 2020, MNRAS, 498, 2239
Harrison, S., Faure, A., & Tennyson, J. 2013, MNRAS, 435, 3541
Hause, M. L., Hall, G. E., & Sears, T. J. 2009, JPCA, 113, 13342
Jackson, W. M. 1974, JChPh, 61, 4177
Knowles, P. J., Werner, H.-J., Hay, P. J., & Cartwright, D. C. 1988, JChPh, 89, 7334
Kozlov, S. V., Stolyarov, A. V., & Pazyuk, E. A. 2024, OptSp, 132, 262
Kulik, H. J., Steeves, A. H., & Field, R. W. 2009, JMoSp, 258, 6
Langhoff, S. R., & Bauschlicher, C. W. J. 1989, ApJ, 340, 620
Lavendy, H., Gandara, G., & Robbe, J. M. 1984, JMoSp, 106, 395
Leach, S. 2012, MNRAS, 421, 1325
Lefebvre, R., & Field, R. 2004, The Spectra and Dynamics of Diatomic Molecules: Revised and Enlarged Edition (New York: Academic), 1
Lin, H.-S., Erickson, M. G., Lin, Y., et al. 1994, CP, 189, 235
Liszt, H. S., & Hesser, J. E. 1970, ApJ, 159, 1101
Liu, L., & Cheng, X. 2022, Comput. Theor. Chem., 1209, 113582
Löhle, S., Wernitz, R., Herdrich, G., et al. 2011, CEAS, 1, 59
Luk, C. K., & Bersohn, R. 1973, JChPh, 58, 2153
McKellar, A. 1940, PASP, 52, 187
Mohamed, K. A., King, G. C., & Read, F. H. 1977, JESRP, 12, 229
Moore, J. H. J., & Robinson, D. W. 2003, JChPh, 48, 4870
Morton, D. C. 2000, ApJS, 130, 403
Mousavi, S. J., Farsani, M. H., Darbani, S. M. R., et al. 2016, ApPhB, 122, 106
Parigger, C. G. 2023, Atoms, 11, 62
Parigger, C. G., Woods, A. C., Surmick, D. M., et al. 2015, AcSpB, 107, 132
Patrascu, A. T., Hill, C., Tennyson, J., & Yurchenko, S. N. 2014, JChPh, 141, 144312
Pupyshev, V. I., Pazyuk, E. A., Stolyarov, A. V., Tamanis, M., & Ferber, R. 2010, PCCP, 12, 4809
Ram, R. S., Wallace, L., & Bernath, P. F. 2010, JMoSp, 263, 82
Rayner, J. T., Cushing, M. C., & Vacca, W. D. 2009, ApJS, 185, 289
Riffel, R., Pastoriza, M. G., Rodríguez-Ardila, A., & Maraston, C. 2007, ApJ, 659, L103
Ritchey, A. M., Federman, S. R., & Lambert, D. L. 2011, ApJ, 728, 36
Roth, K. C., Meyer, D. M., & Hawkins, I. 1993, ApJL, 413, L67
Słyk, K., Bondar, A. V., Galazutdinov, G. A., & Krełowski, J. 2008, MNRAS, 390, 1733
Sneden, C., & Lambert, D. L. 1982, ApJ, 259, 381
Sneden, C., Lucatello, S., Ram, R. S., Brooke, J. S. A., & Bernath, P. 2014, ApJS, 214, 26
Syme, A.-M., & McKemmish, L. K. 2020, MNRAS, 499, 25
Syme, A.-M., & McKemmish, L. K. 2021, MNRAS, 505, 4383
Tennyson, J., Yurchenko, S. N., Al-Refaie, A. F., et al. 2020, JQSRT, 255, 107228

Terashkevich, V. A., Pazyuk, E. A., Stolyarov, A. V., & Yurchenko, S. N. 2022, JQSRT, 292, 108366
Terashkevich, V. A., Pazyuk, E. A., & Stolyarov, A. V. 2021, JQSRT, 276, 107916
Thomson, R., & Dalby, F. W. 1968, CaJPh, 46, 2815
Watson, J. K. G. 2008, JMoSp, 252, 5
Werner, H.-J., Knowles, P. J., Knizia, G., et al. 2012, WIREs Comput. Mol. Sci., 2, 242
Western, C. M. 2017, JQSRT, 186, 221
Wiedemann, G. R., Hinkle, K. H., Keady, J. J., Deming, D., & Jennings, D. E. 1991, ApJ, 382, 321
Yin, Y., Shi, D., Sun, J., & Zhu, Z. 2018, ApJS, 235, 25
Yurchenko, S. N., Al-Refaie, A. F., & Tennyson, J. 2018, A&A, 614, A131
Yurchenko, S. N., Lodi, L., Tennyson, J., & Stolyarov, A. V. 2016, CoPhC, 202, 262